MEASUREMENTS OF 3D TRANSPORT BOUNDARIES WITH URBAN CANOPIES USING MAGNETIC RESONANCE IMAGING

Andrew J. Banko
Civil & Mechanical Engineering
United States Military Academy
752 Thayer Rd, West Point, NY 10996
andrew.banko@westpoint.edu

Ty Homan
Civil & Mechanical Engineering
United States Military Academy
752 Thayer Rd, West Point, NY 10996
ty.homan@westpoint.edu

Michael J. Benson
Civil & Mechanical Engineering
United States Military Academy
752 Thayer Rd, West Point, NY 10996
michael.benson@westpoint.edu

Christopher J. Elkins
Mechanical Engineering
Stanford University
488 Escondido Mall, Stanford, CA 94305
celkins@stanford.edu

ABSTRACT

Measurements of mean flow transport boundaries in a realistic urban canopy model are conducted using magnetic resonance imaging (MRI) techniques. A transport boundary is defined as a ridge of the Finite Time Lyapunov Exponent (FTLE) field computed using the mean velocity. It is found that ridges of the backwards FTLE field, which identify hyperbolic manifolds exhibiting exponential convergence of fluid trajectories, act as barriers to scalar transport. The MRI measurements enable the three-dimensional characterization of transport boundary topology and explain observed cross-wind and vertical scalar transport behaviour. Despite the fact that the FTLE field only guarantees negligibly small mean scalar flux perpendicular to the ridge, the structures appear remarkably robust to turbulent mixing. By contrast, the forwards FTLE field, which describes exponentially separating trajectories, does not inhibit turbulent mixing. This observation is explained by analyzing a simple cellular flow field with both stable and unstable manifolds.

INTRODUCTION

Understanding and predicting turbulent scalar dispersion from street-level sources within the urban canopy is important for determining emergency response, assessing air quality, and providing input to neighborhood and regional scale pollution models. Flow within the canopy is governed by mechanical dispersion due to the mean flow around buildings and turbulent dispersion (Belcher, 2005). The flow topology is fundamentally three-dimensional (3D) and characterized by interacting separation bubbles, convergence zones, and non-equilibrium boundary layers (Britter & Hanna, 2003). These features represent a significant modeling challenge. Laboratory, field data, and high-fidelity simulations have demonstrated non-intuitive plume spread, including up-wind or cross-wind transport and sharp variations in concentration across street intersections (Carpentieri *et al.*, 2012). For instance, Homan *et al.* (2021) describe the interaction of a plume with a 3D urban canopy flow and observe plume displacements larger than the geometric footprint of various buildings. We hypothesize that non-intuitive plume spread is enhanced by mean flow transport boundaries, defined as topological surfaces of the flow field that inhibit scalar transport perpendicular to the boundary. However, these structures are poorly quantified due to limitations of conventional optical- and probe-based measurement techniques.

Experimental advancements using magnetic resonance imaging provide 3D, three-component velocity and passive scalar concentration data on volumetric Cartesian grids (Elkins & Alley, 2007; Banko *et al.*, 2020). These data allow for the quantitative evaluation of flow within complex geometries at millions of points without the need for optical access. The techniques have recently been applied to urban canopy flows (Shim *et al.*, 2019; Homan *et al.*, 2021), and bridge a gap between conventional lab data in idealized urban settings and field data at sparse measurement locations.

Transport boundaries have been previously extracted for oceanic, atmospheric, and biological flows, among others. They are based on the theory of Lagrangian Coherent Structures (LCS), which separate the flow into materially distinct regions (Haller, 2015). One example of an LCS is the Finite Time Lyapunov Exponent (FTLE) field (Shadden *et al.*, 2005). In steady flows, the mass flux perpendicular to an FTLE ridge is negligibly small. Ridges of the FTLE field are therefore suitable candidates for mean flow transport boundaries in urban canopy flows, because they define two-dimensional manifolds (surfaces) with approximately zero mean scalar flux across them.

In this work, we use MRI measurements to quantify the 3D topology of transport boundaries in a realistic urban canopy model. Transport boundaries are extracted as ridges of the FTLE field and compared to measurements of passive scalar dispersion through the canopy.

URBAN CANOPY DATA

Experimental Methods

Experiments are performed on a 1:2206 scale model of the Oklahoma City downtown business district circa 2003 based on the JU2003 field tests. The test section was 3D

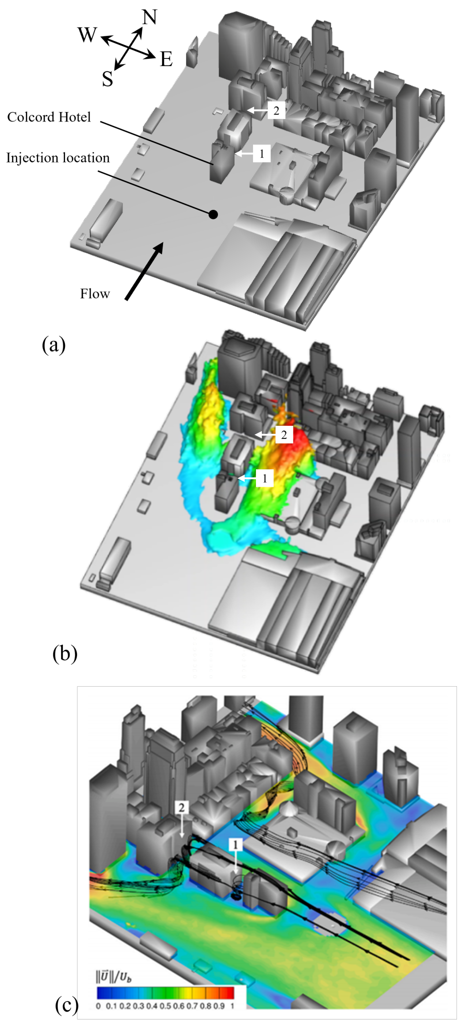

Figure 1. Overview of test section geometry and velocity and concentration data. (a) The urban canopy model. (b) An isosurface of 5% concentration near the end of injection, colored by height. (c) Velocity magnitude on a plane near ground level ($y/H = 0.15$). Streamlines displaying characteristic, 3D flow patterns. Regions of interest 1 and 2 in the building wakes adjacent to the main street and intersection are indicated by the white boxes.

printed using stereolithography and integrated into a water channel with flow conditioning components (diffuser, contraction, and roughness section) to develop a turbulent boundary layer upstream of the urban canopy as described in Homan *et al.* (2021). The main flow direction was from south-to-north as shown in Figure 1(a). The freestream velocity was $U_\infty = 0.3$ m/s and the characteristic building height was $H = 20$ mm, giving a building Reynolds number of $Re_H = 6{,}000$. While well below application scale Reynolds number, the flow within the canopy is fully-turbulent. Moreover, flow separation initiates at the corners of buildings and therefore the large-scale features of the flow are approximately independent of Reynolds number.

A passive scalar is injected at ground level upstream of the Colcord hotel as shown in Figure 1(a). The injection is transient and follows a square waveform with 40% duty cycle and a period of 1 second. The characteristic advection time scale based on the freestream velocity and building height, H,

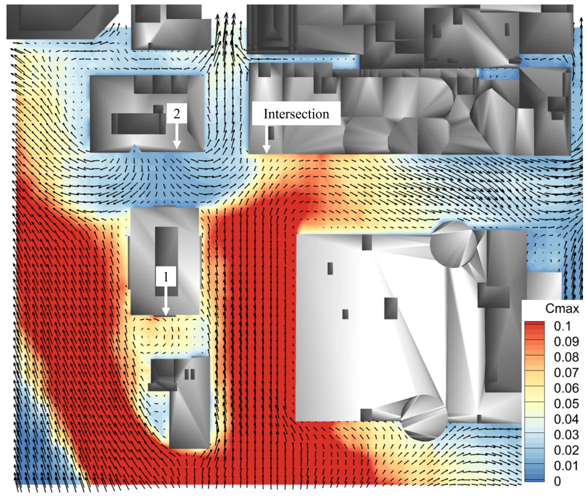

Figure 2. Contours of maximum concentration over the injection cycle with in-plane velocity vectors on a plane near ground level ($y/H = 0.15$). Data shown are the full experimental resolution. Regions 1, 2, and the intersection are indicated by the white boxes.

is $\tau = H/U_\infty = 0.067$ sec. This protocol allows the plume to nearly wash out of the measurement domain between injection pulses.

Measurements of ensemble-averaged velocity and concentration are conducted using magnetic resonance velocimetry (MRV) and magnetic resonance concentration (MRC). Data are acquired on a Cartesian grid of voxels for 12 distinct temporal phases across the injection cycle as described in Homan *et al.* (2021). The reader is also referred to Elkins & Alley (2007) and Banko *et al.* (2020) for detailed descriptions of the techniques. The measurement resolution is 1.5 mm, or approximately 10 voxels per street width. Both MRV and MRC use dilute aqueous solutions of CuSO4 as the working fluid. The uncertainty in velocity is approximately 5% of the freestream velocity. The concentration uncertainty scales with the local concentration level, with a noise floor of about 2% of the injected concentration.

Flow Field Overview

Figures 1(b) and 1(c) provide an overview of the concentration and velocity fields in the urban canopy. Additional details can be found in Homan *et al.* (2021). The concentration isosurface in Figure 1(b) is plotted after the plume has dispersed several city blocks in the streamwise direction. The plume disperses along two distinct paths to the west and east of the Colcord hotel, and several distinct ventilation characteristics are observed between buildings and along street canyons as evidenced by the streamline patterns in Figure 1(c). These include: a recirculation region with vertically oriented vortical motion (region 1), typical of a building wake; the entrainment of freestream fluid downwards into the urban canopy where it spreads at ground level (region 2); and a longitudinal vortex along the extended street canyon. The freestream entrainment in region 2 is due to local variations in building height, similar to a step-up canyon geometry, and shows that the ventilation patterns are geometrically sensitive.

Figure 2 plots contours of the maximum concentration over the course of the injection cycle on a plane near ground level with in-plane velocity vectors. A large concentration gradient bisects the intersection adjacent to region 2. This is due to the convergence of clean freestream fluid spreading at ground level with contaminated fluid transported north from the injector along the large street. Similar phenomena are observed along the west side of region 2 and across the shear layers of separation bubbles next to buildings. The in-plane vector fields in each region suggest a dividing streamline acts as a barrier between the clean and contaminated flow, indicating their importance for the mechanical dispersion of the plume. However, these observations are based on a 2D projection of a 3D flow field. In the following sections, we show that the topology of the 3D flow field forms 2D manifolds that act as transport boundaries.

TRANSPORT BOUNDARY DEFINITION

We define transport boundaries using the theory of Lagrangian Coherent Structures (LCSs). An LCS is a 2D material surface that exhibits normally attracting or repelling fluid trajectories. The mean scalar flux perpendicular to an LCS is zero (or near zero, see numerical computation below). Therefore, LCSs are candidates for transport boundaries within the urban canopy because their properties agree with our qualitative overview of the velocity field and its effect on contaminant dispersion. We focus primarily on LCSs defined from the FTLE field and also make comparisons to the Stationary LCSs (SLCSs) described in Teramoto *et al.* (2013).

The FTLE field is computed from the deformation gradient tensor of the flow map $\phi^T(\mathbf{x}_o)$, obtained by integrating the system of equations $d\phi^t/dt = \mathbf{U}$ over a finite time interval, T. Here, $\mathbf{x_o}$ is the initial position of fluid particles and $\mathbf{U}$ is the mean velocity vector field. In other words, $\phi^T(\mathbf{x}_o)$ is the final positions of fluid particles originating at $\mathbf{x_o}$ after a time T. Denote the deformation gradient tensor by $\mathbf{D}_{\mathbf{x}_o}\phi^T$, and let λ_i^T and ζ_i^T be the i^{th} eigenvalue and eigenvector of the Cauchy-Green strain tensor, $C^T = (\mathbf{D}_{\mathbf{x}_o}\phi^T)^*(\mathbf{D}_{\mathbf{x}_o}\phi^T)$, where $(\cdot)^*$ indicates the transpose. Then, the FTLE field is given by $\sigma^T = \ln(\sqrt{\max(\lambda_i)})/T$. Integration forwards in time determines the forwards FTLE field corresponding to exponentially separating trajectories. Integration backwards in time determines the backward FTLE field corresponding to exponentially converging trajectories.

Figures 3(a) and 3(b) plot the forwards and backwards FTLE fields computed from the experimental mean velocity field on a plane near ground level. A 4^{th} order Runge-Kutta temporal integration scheme and linear spatial interpolation for the velocity are used to compute the particle trajectories. Initial positions for the fluid particles are seeded on a uniform Cartesian grid with an isotropic spacing of Δx = 0.3 mm. The velocity outside the fluid domain is set to zero. The total integration time is $T = 2H/U_\infty$ and the time step is $\Delta t = \Delta x/(4\cdot\max(|\mathbf{U}|))$. Second order central differencing is used to compute the deformation gradient tensor. Ridges, or local extrema within the wall-normal plane, are nearly parallel to the in-plane velocity vectors. Therefore, the mean flux across a ridge is small, at least in the 2D projection.

The flux across a ridge is made quantitative in 3D by comparing the FTLE fields to the Stationary LCSs described in Teramoto *et al.* (2013). An SLCS is the set of points satisfying: (1) $L^T \equiv \zeta_1^T\cdot\mathbf{U} = 0$, (2) $\lambda_2^T < \varepsilon^2\lambda_1^T$ and $\lambda_1^T > 0$, and (3) $|\cos^{-1}(|\zeta_1^T\cdot\mathbf{n}|)| \le \alpha$. Subscripts 1 and 2 denote the largest and second largest eigenvalues, respectively, and the corresponding eigenvectors. Condition (1) guarantees that the direction of maximal particle separation (or attraction backwards in time) is orthogonal to the local flow direction. Condition 2 ensures that rate of separation (attraction) normal to the SLCS dominates the rates of separation (attraction) in other directions. Condition 3 enforces that the flux perpendicular to the SLCS can be made small by controlling the parameter α. Here, $\mathbf{n}$ is the unit normal to the SLCS computed from the gradient of L^T.

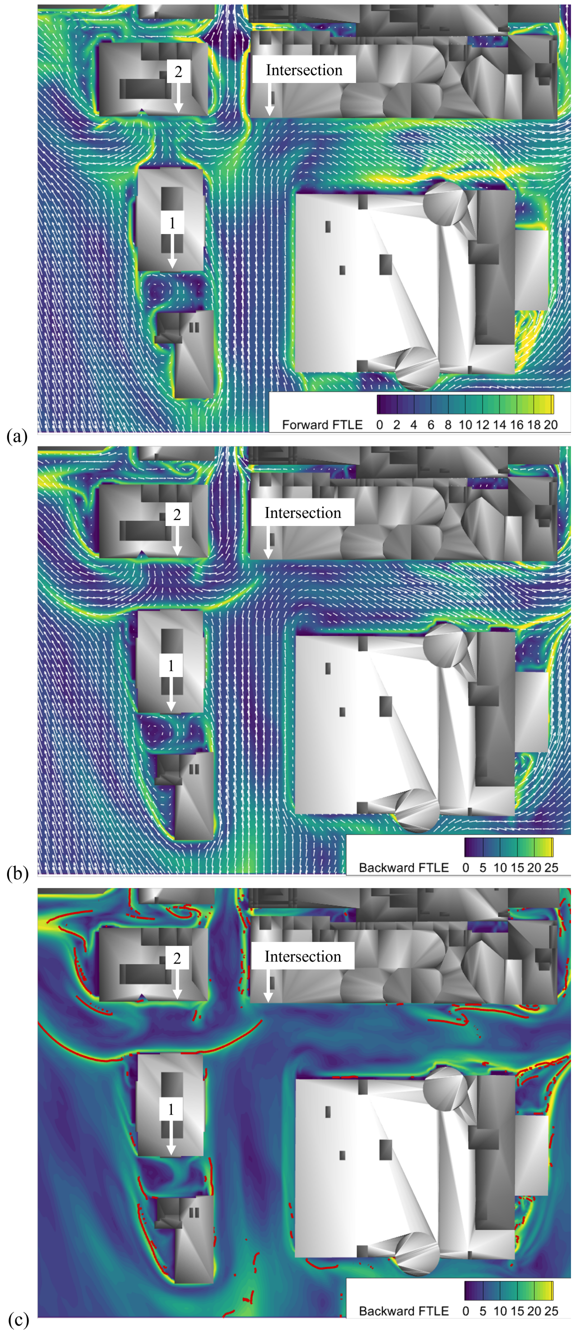

Figure 3. Contours of the FTLE field on a plane near ground level ($y/H = 0.15$) for (a) forwards-in-time and (b) backwards-in-time integration. (c) A comparison between the contours of the backwards FTLE field and the SLCS shown in red.

Figure 3(c) overlays the backwards SLCS (red) on contours of the backwards FTLE field. The SLCS parameters are $\varepsilon = 0.2$ and $\alpha = 25^o$. Note the close correspondence between ridges of the FTLE field and the SLCS. Figure 4 plots the probability distribution (PDF) of the angle between the unit normal vector to the SLCS and the mean velocity vector. The majority of points are concentrated around 90^o, indicating near zero flux across the SLCS. Therefore, the flux across FTLE ridges

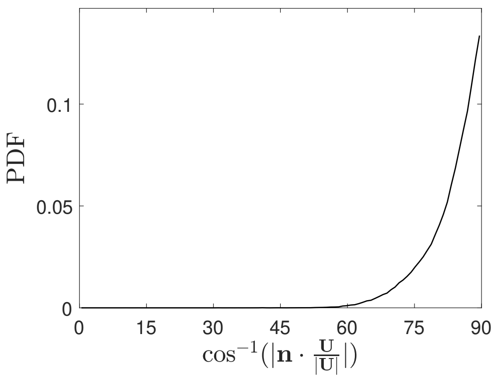

Figure 4. Probability distribution of the angle between the normal vector to the SLCS and the local velocity vector.

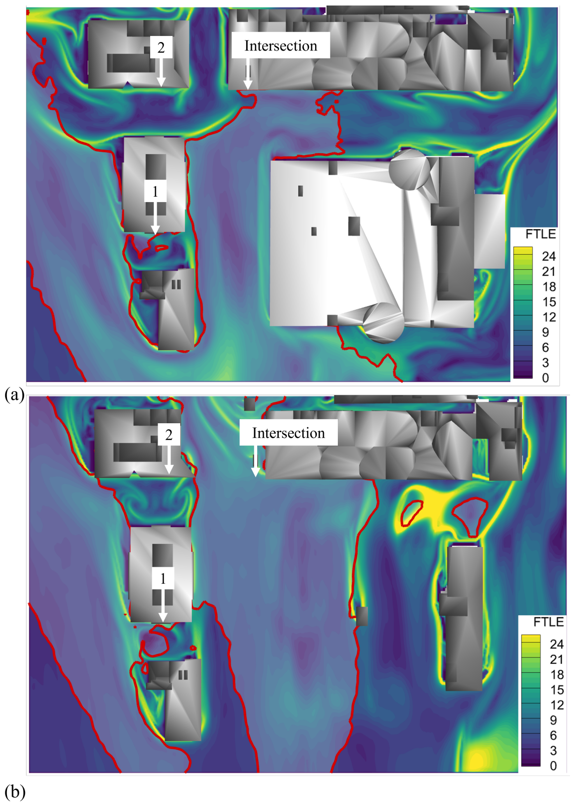

Figure 5. Contours of the backwards FTLE field overlaid with a 3% maximum concentration isocontour (red). The interior of the contour is shaded for clarity. (a) A plane near ground level ($y/H = 0.15$). (b) A plane near $y/H = 0.5$.

is near zero as well. Future work will investigate the effect of experimental uncertainty on the flux. For the remainder of the paper, we define LCSs by thresholding the FTLE fields to large values.

TRANSPORT BOUNDARY EFFECTS ON 3D DISPERSION PATTERNS

The FTLE ridges in Figure 3 coincide with the convergence zones, separation bubbles, and stagnation points described previously. These structures extend outwards into the flow field by a distance similar to the characteristic building length scales. This is particularly evident for the backwards

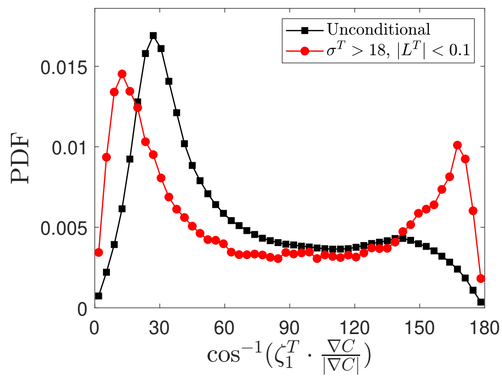

Figure 6. Probability disbtribution of the angle between the maximum convergence direction and the average concentration gradient. PDFs are computed for the entire flow field and conditioned on proximity to an FTLE ridge.

FTLE ridges. For example, the separation bubbles adjacent to buildings are bounded by an FTLE ridge that extends the entire building length in the streamwise direction. Likewise, the freestream flow which spreads at ground level in region 2 is bounded by FTLE ridges which extend a full building width to the east and west. The eastern ridge bisects the intersection, as was qualitatively discussed above. These topological structures have a significant impact on the concentration field and are robust to turbulent mixing as shown below.

Conversely, the forwards FTLE ridges are typically located close to building corners and do not penetrate as deeply into the flow field. Forwards FTLE ridges intuitively terminate at building corners since they demarcate diverging fluid trajectories. It is observed that forward FTLE ridges do not suppress turbulent dispersion of the plume, and are therefore less efficient transport boundaries. For brevity, we focus on the backwards FTLE field in the remainder of this section. The final section of the paper describes a model system for understanding the relative importance of turbulent mixing across backwards and forwards FTLE ridges.

Backwards FTLE Results

Figure 5 illustrates the spatial correspondence between the backwards FTLE ridges and the concentration field. FTLE contours on wall parallel planes are overlaid with a 3% isocontour of maximum concentration. The plane near ground level shows that little contaminant mixes across the ridges bounding the separation bubble on the west side of the Colcord Hotel. The FTLE ridge which bisects the intersection also separates clean and contaminated fluid, and redirects the plume eastward as previously described. The ridge on the west side of region 2 nominally separates clean and contaminated fluid, but the concentration isocontour crosses a portion of the FTLE ridge. In fact, this is partly due to 3D mean flow effects as described in the following section.

A plane halfway up the Colcord hotel shows similar correlations between the backwards FTLE ridges and the boundaries between clean and contaminated fluid. Notably, closed FTLE contours on the east side of the measurement domain enclose contaminated fluid that is transported vertically out of the street canyon in the tall building wakes.

Figure 6 summarizes these observations by plotting the PDF of the angle between the maximum convergence direction (eigenvector ζ_1^T) and the average concentration gradient.

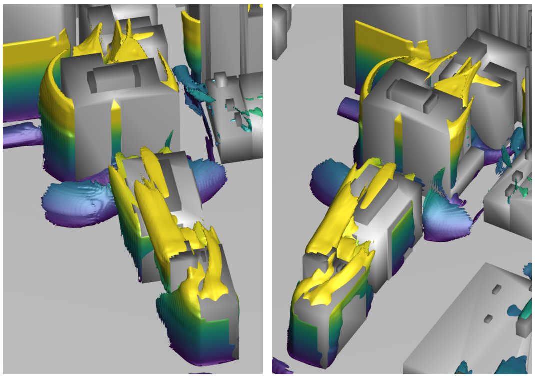

Figure 7. Isosurfaces of the backwards FTLE field colored by height. The isosurface level is $\sigma^T = 20$. Two isometric views are shown.

When conditioned on proximity to an FTLE ridge, the PDF becomes peaked towards angles of 0^o and 180^o. This indicates that the concentration gradient is preferentially aligned with the direction normal to the FTLE ridge. In other words, the concentration increases or decreases most rapidly moving across the ridge. Therefore, the FTLE ridges act as transport boundaries which inhibit scalar flux normal to their surface.

3D Flow Topology

Figure 7 shows isosurfaces of the FTLE field colored by height within the urban canopy to show the 3D structure of the surfaces. Sheet-like structures demarcate the separation bubbles on the sides of buildings. The boundaries generated by the entrained flow within region 2 are curved and impact the vertical plume transport in addition to its lateral dispersion. Figure 8 illustrates this behaviour by plotting contours of peak concentration on a streamwise vertical plane that cuts through the FTLE extending into the intersection. The plume is deflected vertically over the intersection structure creating a bubble of clean flow near the ground that is eventually filled in by wall-normal mixing downstream of the intersection.

Two additional streamwise vertical planes cutting through the western FTLE surface are also depicted in Figure 8. The maximum concentration contours again show that the plume is dispersed vertically by the transport boundary. Due to the downstream building and the FTLE surface generated by this building's separation bubble, the contaminated flow is advected back towards ground level on the downstream side of the FTLE surface and recirculates upstream. Therefore, the downstream side of the transport boundary experiences dilute concentrations due to turbulent mixing across the ridge, but also due to mean advection by the complex 3D flow. This explains the why the concentration contours cross the FTLE ridge in Figure 5.

A Model System for Understanding Turbulent Dispersion

The turbulent scalar flux through the FTLE surfaces is not necessarily zero because the FTLE is defined using the mean velocity field. Yet, observations suggest that the turbulent flux is small, especially for the backwards FTLE field. This could be because turbulent fluctuations which cross the transport boundary are advected by the strong convergence flow back towards the boundary, keeping contaminated flow near the hyperbolic manifolds. Figure 9(a) shows a diagram of this process. Conversely, exponentially separating trajectories of the forwards FTLE field would amplify the effects of turbulent dispersion across the FTLE surfaces.

A simple cellular flow field is constructed to illustrate this hypothesis. Consider the mean velocity field defined by $U = -\sin(2\pi x)\cos(2\pi y)$ and $V = \cos(2\pi x)\sin(2\pi y)$ on the unit square $x \in [0,1]$ and $y \in [0,1]$. This flow field forms four recirculating cells separated by the line $x = 0.5$ (a stable manifold), and the line $y = 0.5$ (an unstable manifold). Additional stable and unstable manifolds can similarly be identified along the domain boundaries. A passive scalar is initialized at 100% concentration in one quandrant of the domain and allowed to advect and diffuse over a time $T = 1$. The scalar diffusivity is $D = 0.0025$. This implies a diffusion length scale of $l_D \equiv \sqrt{D \cdot T} = 0.05$, or 5% of the domain. A no-flux condition is applied at the domain boundaries.

Figure 9 plots the final concentration field overlaid with velocity vectors. The scalar diffused across both the stable and unstable manifolds, but the net flux perpendicular to the stable manifold is reduced due to the converging flow. Therefore, the concentration gradient remains large near the central stagnation point. Concentration which diffuses across the unstable manifold is eventually advected away from either side of the downstream stagnation points and disperses rapidly into the adjacent quadrants. In fact, a comparison of Figures 3 and 5 show evidence of this behavior in the wake of the Colcord Hotel. Contaminant is transported across the forwards FTLE ridge extending from the downstream building corner and fills region 1.

CONCLUSIONS

The effect of 3D flow topology on passive scalar dispersion within a realistic urban canopy model was studied experimentally. Magnetic resonance imaging was used to obtain volumetric fields of ensemble-averaged velocity and concentration for a transient release in a scale model of the Oklahoma City downtown business district circa 2003. Mechanical dispersion of the plume was enhanced due to the presence of mean flow transport boundaries. Transport boundaries correspond to 2D manifolds with zero mean scalar flux, formed by the global topology of the flow field.

Two different definitions were considered based on the theory of Lagrangian Coherent Structures and computed from the MRI data: the Finite Time Lyapunov Exponent Field (FTLE) and the Stationary Lagrangian Coherent Structure (SLCS). Ridges of the FTLE field agree with zero level sets of the SLCSs, and were shown to have small mean flux normal to the surfaces. Deviations from zero mean flux are likely due to experimental uncertainty and resolution, and will be a topic of future investigation.

The backwards FTLE field was correlated with sharp gradients in the concentration field and forms transport boundaries in the urban canopy. The MRI measurements provided unique insight into the 3D structure of the FTLE surfaces and their effect on dispersion. Prominent features included the shear layers bounding separation bubbles around buildings and regions of strong flow convergence due to complex ventilation patterns induced by the heterogeneous urban geometry. Both lateral and vertical dispersion were enhanced due to the deflection of the main plume by these structures.

While the backwards FTLE surfaces were remarkably robust to turbulent mixing, the forwards FTLE surfaces did not clearly demarcate clean and contaminated fluid. This observation was explained by analyzing the dispersion of a diffusive passive scalar contaminant in a cellular flow field.

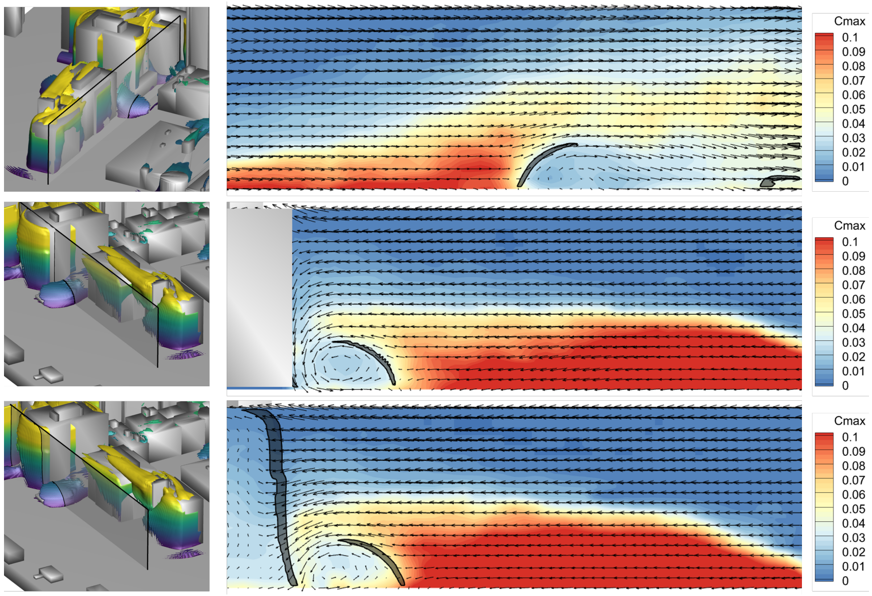

Figure 8. Contours of maximum concentration on streamwise vertical planes with in-plane velocity vectors. Isocontours of the backwards FTLE field at $\sigma^T = 20$ are shown in black. Locations of each plane are shown in the left-hand-side subfigures.

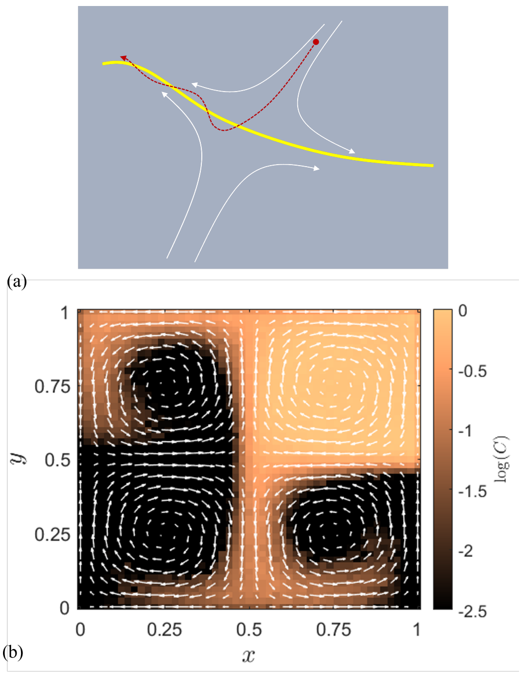

Figure 9. Model for turbulent diffusion across hyperbolic Lagrangian coherent structures. (a) Illustration of the pathline for a fluid element near a stable manifold. (b) Cellular flow field with passive scalar advection and diffusion.

Future work will assess the prevalence of transport boundaries across a wider variety of urban canopy flow datasets developed by the authors using MRI. Studies using large eddy simulations (LES) or conventional optical experimental techniques could focus on the turbulence dynamics near the mean flow transport boundaries. MRI data provide rigorous validation cases for LES and also identify regions of interest within complex, 3D flow fields for additional experiments. Finally, identifying transport boundaries may be important for future model development, because models must accurately predict their locations in order to capture mechanical dispersion.

REFERENCES

Banko, Andrew J, Benson, Michael J, Gunady, Ian E, Elkins, Christopher J & Eaton, John K 2020 An improved three-dimensional concentration measurement technique using magnetic resonance imaging. *Exp. Fluids* **61** (2), 1–19.

Belcher, Stephen E 2005 Mixing and transport in urban areas. *Philosophical Transactions of the Royal Society A: Mathematical, Physical and Engineering Sciences* **363** (1837), 2947–2968.

Britter, RE & Hanna, SR 2003 Flow and dispersion in urban areas. *Annual review of fluid mechanics* **35** (1), 469–496.

Carpentieri, Matteo, Hayden, Paul & Robins, Alan G 2012 Wind tunnel measurements of pollutant turbulent fluxes in urban intersections. *Atmospheric Environment* **46**, 669–674.

Elkins, Christopher J & Alley, Marcus T 2007 Magnetic resonance velocimetry: applications of magnetic resonance imaging in the measurement of fluid motion. *Experiments in Fluids* **43** (6), 823–858.

Haller, George 2015 Lagrangian coherent structures. *Annual Review of Fluid Mechanics* **47**, 137–162.

Homan, Ty A, Benson, Michael J, Banko, Andrew J, Elkins, Christopher J, Chung, Daniel H, Rhee, Joshua, Mooradian, Lynne D & Eaton, John K 2021 Magnetic resonance imaging measurements of scalar dispersion for a scaled urban transient release. *Building and Environment* **205**, 108163.

Shadden, Shawn C, Lekien, Francois & Marsden, Jerrold E 2005 Definition and properties of lagrangian coherent structures from finite-time lyapunov exponents in two-dimensional aperiodic flows. *Physica D: Nonlinear Phenomena* **212** (3-4), 271–304.

Shim, Gawoon, Prasad, Dipak, Elkins, Christopher J, Eaton, John K & Benson, Michael J 2019 3d mri measurements of the effects of wind direction on flow characteristics and contaminant dispersion in a model urban canopy. *Environmental Fluid Mechanics* **19** (4), 851–878.

Teramoto, Hiroshi, Haller, George & Komatsuzaki, Tamiki 2013 Detecting invariant manifolds as stationary lagrangian coherent structures in autonomous dynamical systems. *Chaos: an interdisciplinary journal of nonlinear science* **23** (4), 043107.